

1 **1.2-million-year band of Earth–Mars obliquity modulation on the**
2 **evolution of cold late Miocene to warm early Pliocene climate**

3

4 Jie Qin^{1,2}, Rui Zhang^{1,2*}, Vadim A. Kravchinsky^{1,2, *}, Jean-Pierre Valet^{1,3}, Leonardo
5 Sagnotti⁴, Jianxing Li⁵, Yong Xu⁶, Taslima Anwar^{1,2}, Leping Yue¹

6

7 ¹ Institute of Cenozoic Geology and Environment, State Key Laboratory of Continental
8 Dynamics, Department of Geology, Northwest University, 710069 Xi'an, China

9 ² Geophysics, Department of Physics, University of Alberta, T6G2E1 Edmonton, Canada

10 ³ Institut de Physique du Globe de Paris, 75238 Paris cedex 05, France

11 ⁴ Istituto Nazionale di Geofisica e Vulcanologia, 00143 Roma, Italy

12 ⁵ Chengdu Center of Geological Survey, Geological Survey of China, 610081 Chengdu,
13 China

14 ⁶ Xi'an Center of Geological Survey, China Geological Survey, 710054 Xi'an, China

15 * e-mails: ruizhang@nwu.edu.cn (R.Z.), vadim@ualberta.ca (V.A.K.)

16 **Abstract**

17 The climatic transitions during the Miocene–Pliocene epochs had significant impacts on
18 the worldwide biological diversity and were associated with large turnovers of continental
19 vegetation and fauna. Previous studies have shown that late Miocene cooling and
20 continental aridification which was initiated 7 Ma reversed to warm conditions across the
21 Miocene–Pliocene Boundary ~ 5.3 Ma. Here we present detailed orbital pacing of Asian
22 monsoon deposits to constrain further the global climate change during this period. We
23 produce high-resolution magnetic susceptibility records which reveal that the 1.2 Myr
24 obliquity modulation would have been the main driving factor of the cooling and warming
25 that occurred ~ 7 Ma and 5.3 Ma, respectively. The Tibetan rise and closures of the Panama
26 and Indonesian seaways enhanced the impact of the 405 kyr eccentricity cycles to an
27 oscillatory climatic state while the Northern Hemisphere glaciations were increasing from
28 4 to 2.5 Ma.

29

30 **Plain Language Summary**

31 For the first time, we point out eolian sediments from Chinese Loess Plateau through the
32 Asian monsoon is primarily respond to the long-period evolving dynamics of Earth-Mars
33 obliquity modulation since the late Miocene. Our study deciphers the presence of
34 oscillatory sedimentary patterns resulting from the 1.2-million-year band were responsible
35 for the global climate transition during the aridification and cooling at ~ 7 Ma and warming
36 at ~ 5.3 Ma. Our new discovery challenges the previous hypothesis that carbon circulations
37 involving both the marine and terrestrial carbon reservoirs were instrumental in driving
38 late Miocene climate cooling and warming, which provide a valuable analog for the
39 climate prediction of Pliocene-like temperature level in the coming decades.

40

41 **1. Introduction**

42 In the late Miocene, terrestrial environments and ecosystems have undergone tremendous
43 changes due to the presumed decline of atmospheric CO₂ between 8 and 6 Ma (Beerling
44 et al., 2011; Bolton and Stoll, 2013). This period has seen the replacement of large areas
45 of tropical and subtropical forests by deserts (such as Sahara Deserts) and the expansion
46 of C₄ grassland (Cerling et al., 1997; Schuster et al., 2006; Huang et al., 2007). The large
47 restructuring of vegetation and landscape coincided with major turnovers in animal
48 communities (Badgley et al., 2008). However, those continental environmental upheavals
49 do not bring direct information on the temperature change during the Late Miocene
50 (Herbert et al., 2016). The marine isotope record younger than the middle Miocene is
51 characterized by periodic anomalies of the Antarctic ice volume that have been shown to
52 be probably driven by obliquity in marine sequences from the peri-Antarctic margin
53 (Naish et al., 2009). No clear trend suggests a long-term climatic change during the late
54 Miocene (Zachos et al., 2001; Lewis et al., 2008; Westerhold et al., 2020). Recently, the
55 integration of marine sea-surface temperature (SST) made it possible to estimate the
56 evolution of global temperature during the Miocene (LaRiviere et al., 2012; Herbert et al.,
57 2016). The late Miocene cooling did not lead monotonically to the ice age in the northern
58 hemisphere that prevailed through most of the Pliocene (LaRiviere et al., 2012).
59 Furthermore, temperature proxies indicate that cooling (Ravelo et al., 2004; Dowsett et al.,
60 2005; Fedorov et al., 2006) and aridification (Lawrence et al., 2006) ceased during the
61 Pliocene and that warmer conditions occurred after 5.3 Ma. Because the present-day global
62 warming may induce Pliocene-like temperatures during the next decades, a good

63 knowledge of the transition from a cold late-Miocene and warm early-middle Pliocene
64 climate may provide a valuable analog for climatic projections (Burke et al., 2018).

65 It remains uncertain whether there is a link between contemporaneous atmospheric
66 circulation, ecosystem changes in continental environments and the orbital variation
67 effects recorded by climate proxies from the ocean realm. The hundreds of thousand-years'
68 time scale low-latitude processes such as monsoon forcing on the upper-ocean circulation
69 and its productivity strongly influence climate dynamics and constrain the reconstruction
70 of ice volume and atmospheric greenhouse gas concentrations (Holbourn et al., 2018). The
71 high topography of the Tibetan-Pamir Plateau contributes to amplifying the Asian
72 monsoon system that controls precipitation as well as the level of convection (An et al.,
73 2001; Boos and Kuang, 2010). During the Quaternary, the climate was mostly affected by
74 variability of precessional insolation modulated by the 405 and 100 kyr eccentricity cycles
75 and the 41 kyr obliquity band (Nie et al., 2008; Hao et al., 2012; Nie, 2018; Sun et al.,
76 2019). In earlier records from the late Miocene to Pliocene, some may show
77 unconventional cycles related to the orbital inclination rates of Earth and Saturn, called
78 173 kyr metronome for Asian monsoon, which arouses our interest (Zhang et al., 2022).

79 From the analysis of the obliquity solution, both the 173 kyr and 1.2 Myr obliquity bands
80 are of particular importance, the signal from the second is even stronger than that of the
81 first one (Laskar, 2020). In order to detect the longer orbitally forced cycle that has not
82 been studied in the monsoon region, and to estimate whether it is associated with critical
83 late Miocene-Pliocene climate transitions, we choose the eolian red clay deposits as the
84 research subject.

85

86 **2. Material and methods**

87 **2.1 Material**

88 The monsoonal system is primarily characterized by intense summer rainfall over a wide
89 area that lies along the continental-ocean pressure gradient and brings rainfall onto the
90 continent (An et al., 2001; Sun et al., 2019). The East Asian monsoon (EAM) controls the
91 amounts of precipitation and dust brought from the Indian Ocean to the Pacific Ocean by
92 seasonal changes of warm moist air. Dry winds from the Asian high latitudes transported
93 dust that yielded the formation of the Chinese Loess Plateau (CLP) (Hao et al., 2012)
94 (Figure 1a). The Liulin (LL) eolian red clay section (N37°21', E110°45') is flanked to the
95 east by the Lüliang Mountains and to the west by the Yellow River, dozens of kilometers
96 away from the large mountain ridges (Figure 1b). The 68-meter thick wind-blown deposits
97 consist of brownish-red clay with sporadic and smaller caliche nodules (<5 cm) and
98 abundant Fe–Mn coatings at the top intercalated by carbonate horizons. The bottom of the
99 wind-blown deposits in the LL section was dated late Miocene by comparing the
100 *Hipparion* teeth discovered at 56.3 m in the LL section with the analogous fossil layers in
101 the neighboring Wujiamao and Fuxing sections (Xu et al., 2013; Zhang et al., 2022). This
102 constraint enabled us to establish a first chronology of the LL section after correlating the
103 magnetostratigraphic data to the geomagnetic polarity timescale (GPTS) (Ogg, 2012).

104

105 **2.2 Methods**

106 2.2.1 Sampling and Laboratory Measurements

107

108 30 samples at 2 m stratigraphic spacing were selected for thermomagnetic analyses using
109 an MFK2 Kappabridge with a CS-4 furnace under an argon atmosphere to prevent
110 oxidation during heating. Oriented paleomagnetic samples ~ every 10 cm and cut into 2
111 cm thick cubes for paleomagnetic measurements. A total of 618 samples were measured
112 at 20 cm, increased to 10 cm in the parts where polarity reversals were more frequent. The
113 samples were stepwise demagnetized every 50°C from room temperature up to 600°C
114 using an MMTD 80 thermal demagnetizer. The natural remanent magnetization was
115 measured using either a spinner JR6-A magnetometer or a 2G-755 magnetometer located
116 in a low magnetic field space (<100 nT). The directions of the characteristic remanent
117 magnetization were estimated by principal component analysis (Krischvink, 1980). Only
118 determinations with maximum angular deviation (MAD) below 10° were accepted.

119 The magnetic susceptibility (MS) of powdered samples was measured using a Bartington
120 MS-2 susceptibility meter. Grain size (GS) analysis was performed with a Mastersizer
121 2000 laser particle analyzer. 0.2 g powder samples were first treated with 10% H₂O₂ for
122 about 15 min to remove organic matter and to ensure that the excess peroxide was
123 destroyed. Carbonate was removed using a 10% boiling HCl solution of 10ml and the
124 samples were dispersed for 15 min. with 10 ml 10% Na(PO₃)₆ in an ultrasonic bath prior
125 to the measurements. We performed a cyclostratigraphy analysis through spectral analysis
126 of the MS and GS stratigraphic trends. We repeated the procedure to generate several new
127 correlations between the magnetic polarity zones and the GPTS till the orbital periods were
128 resolved clearly in the MS and GS stratigraphic trends.

129

130 **2.2.2 Spectral Analysis**

131

132 Spectral analysis was applied to check the occurrence of Milankovitch periodicities in MS
133 and GS trends by attempting several correlations between each magnetic polarity pattern
134 and the GPTS (Anwar et al., 2015; Zhang et al., 2021). Wavelet analysis with 95%
135 confidence level of background red noise was used to calculate the spectra of the MS and
136 GS records (Torrence and Compo, 1998). Before spectral analysis, we removed the long-
137 term trends by subtracting a fitted smooth line in order to minimize the effects of non-
138 orbital periods. We established initial magnetostratigraphy and then generated several
139 correlation patterns between each magnetic polarity pattern and the GPTS until the best
140 orbital bands were clearly observed. After confirming the magnetostratigraphy, both 405-
141 kyr and 100-kyr cycles were extracted by filtering bands at the same time (with two
142 bandwidths of 350–500 kyr and 80–125 kyr separately) in Matlab. Coherence between the
143 band-pass filtered MS and eccentricity was scrutinized by calculating a correlation
144 coefficient between the two-time series at zero phase using Matlab codes throughout the
145 late Miocene – early and middle Pliocene. We shifted the MS curve towards younger or
146 older ages by ~ 30 to 200 kyr steps that were imposed by the coherency analysis in order
147 to maximize the coherency between the two-time series with a zero-time lag; then, a new
148 time series could be obtained from the tuning process. The process was repeated many
149 times until each peak of the two curves matched well and the correlation coefficient at
150 zero-time lag reached the maximum. Midway in the process, for a very small time lag
151 between the two series, we stretched or squeezed the MS curve manually to make it match

152 the eccentricity. Each tuned timescale was also applied to GS records at the same time.
153 The spectral powers were produced to help determine our final age model.

154

155 **3. Results**

156 **3.1 Rock magnetism and magnetostratigraphy**

157

158 The plots of MS (χ) versus temperature (T) show that the heating and cooling cycles are
159 nearly reversible (Figure 2). The sharp drop of χ between $\sim 400\text{--}585$ °C, indicates the
160 presence of magnetite. Further decrease of χ to 700 °C reveals that hematite is also present.
161 Representative demagnetization results for different depths are shown in Figure 3 with
162 orthogonal vector diagrams. Our demagnetization results demonstrated that the low-
163 temperature overprints generally ranged from room temperature to 200 °C. After the
164 elimination of the low-temperature component, the samples yielded a stable characteristic
165 remanent magnetization (ChRM) tending to the origin.

166 Paleomagnetic analysis reveals five normal (N1 – N5) and five reversed (R1 – R5) polarity
167 intervals from the reliable ChRM directions (Figure 4). All magnetostratigraphic intervals
168 are established based on more than 4 coinciding samples (and over at least 0.8 meters in
169 the depth) to exclude the effects from small amplitude and short period anomalies (Zhang
170 et al., 2018; Zhang, Kravchinsky, et al., 2021, Zhang, Wei, et al., 2021 Zhang et al., 2022).
171 Three brief normal polarity events (less than or equal to 4 coinciding samples and less than
172 0.8 m in thickness) were also verified from the ChRM recording (red horizons in Figure
173 3). Sand, gravel and mammalian fossils found in the lower part of the section show

174 negligible significant influence from alluvial processes (Figure 4a). The dense carbonate
175 layers and mudstone indicate that the rainwater during the uplift of the Lüliang Mountains
176 was not only in the form of surface flow but could also enrich the groundwater horizons.
177 Groundwater is capable of reducing the iron oxides causing substantial re-magnetization
178 of the eolian sediments. We marked five prominent layers, that could be affected by the
179 groundwater, with light green shading in Figure 4.

180 The fossils found from sandy layers at 56.3 m in the depth of the section containing the
181 *Hipparion* fauna were dated between 7.2 and 6.8 Ma at the adjacent Fuxing section, 7.0–
182 6.7 Ma at the Wujiamao and Baode sections (Zhu et al., 2008; Xu et al., 2013; Zhang et
183 al., 2022). Here, *Hipparion* teeth are thought to be ~ 6.8 Ma in the magnetostratigraphy
184 when N5 and R5 are correlated to C3An and C3Br. This constraint enabled us to establish
185 the first chronology after correlating the magnetostratigraphic data to the geomagnetic
186 polarity timescale (GPTS) (Ogg, 2012). Following the visual correlation, N1 – N3 are
187 associated with C3n.1n – C3n.3n while a brief normal event remains a question mark with
188 respect to C3n.4n. In the field observation, dense calcareous nodules, mudstone and
189 carbonate layers developed from 18 – 27 m, which means underneath the short polarity
190 record at ~18 m, records of rising groundwater flows had been continuously superimposed
191 in the stratum from 27 m and above. Such rework could have disrupted the original ChRM,
192 causing the remagnetization to obscure the previous record. The lower two events at ~ 60
193 m from the section are only recorded in the sandy layer. As paleomagnetic samples in the
194 sand are likely acquired viscous magnetic fields through remagnetization, further
195 verification of the authenticity is required for these question marked red horizons (Zhang
196 et al., 2018; Zhang, Kravchinsky, et al., 2021; Zhang, Wei, et al., 2021; Zhang et al., 2022).

197 Considering dense carbonate and sandy layers developed at the depth of 41–46 m, it
198 indicates that groundwater might also affect the remnant magnetization of the N4 polarity
199 zone. In this case, only N1, N2, N3 and N5 can be used for the initial targeting age prior
200 to tuning to the orbital parameters. Then, we performed a cyclostratigraphy analysis
201 through spectral analysis of the MS and GS records. To verify the correctness of our
202 magnetostratigraphic correlation we generated several new correlations between the
203 magnetic polarity zones and the GPTS and performed spectral analysis until the orbital
204 periods were clearly resolved in the MS and GS records. Clear peaks of the 405 kyr
205 eccentricity band can be observed between 7 and 5.4 Ma (Figure. 5A and 5C). The 100
206 kyr cycles can also be identified at around 6.2–6 Ma in the MS spectrum even though their
207 power amplitudes were much weaker than the 405 kyr power (Figure 5A). Analogously, a
208 relatively low-amplitude 100 kyr cycle revealed between 5.9 and 5.7 Ma in the GS
209 spectrum (Figure 5C). The final magnetostratigraphic correlation that incorporated the
210 cyclostratigraphic procedure described in Methods is shown in Figure 4.

211

212 **3.2 Orbital tuning and astronomical calibration**

213

214 Once the magnetostratigraphic age of the LL section has been compatible with the
215 cyclostratigraphy, we conducted two-channel-band filtering (405 kyr and 100 kyr) for both
216 MS and GS data to highlight the visibility of the eccentricity band and tunes the filtered
217 record cycle-by-cycle to the long eccentricity maxima (405 kyr) and short eccentricity
218 maxima (100 kyr) at the same time (Figure 5). To examine the coupling between our

219 records and eccentricity cycles, we calculated the correlation coefficient between filtered
220 MS and eccentricity at zero phases. Then we shifted the filtered MS curve to the left or
221 right at a short time span implied by the coherency analysis in order to fit it with the filtered
222 eccentricity 405 kyr until the correlation coefficient was maximized. After that, we carried
223 out fine adjustments to the stronger 100 kyr cycle improving further the correlation
224 coefficient. We repeated this procedure until the curve matching and correlation
225 coefficients were maximized. During the tuning processes, we also adjusted some small-
226 time lags between the two series, by stretching or squeezing the MS peaks to the
227 eccentricity peaks (Figure 5B). The final astronomical calibration based on the MS turning
228 was applied to the GS record (Figure 5D).

229 The calculated sedimentation rate (Figure 6) varied from 1.6 to 3.6 cm/kyr with an average
230 of 2.2 cm/kyr. These values are typical of the eolian red clay dust in the CLP (e.g. Nie et
231 al., 2008; Anwar et al., 2015; Zhang et al., 2018).

232

233 3.3 Stratigraphic correlations

234

235 To investigate large-scale climate variations we first compare the LL section to the
236 classical Jingchuan section (JC) which is located in the middle of CLP (Ding et al., 2001),
237 and the adjacent Shilou (SL) section which is situated close to LL and stratigraphically
238 continues LL to the younger age until 2.6 Ma (Ding et al., 2001; Anwar et al., 2015)
239 (Figure 7). Further comparisons to the eastern and western edges of CLP can be found in
240 Supplementary Fig. 1.

241 The bottom age of the SL section was extensively debated and assigned from the late
242 Miocene at 11 Ma (Xu et al., 2009, 2012), 8 Ma (Ao et al., 2016; 2018), to the early
243 Pliocene at 5.2 Ma (Anwar et al., 2015; Zhang, et al., 2018, 2022). Both Xu et al. (2012)
244 and Ao et al. (2016, 2018) mistakenly assigned the finding of micromammal *Meriones* sp.
245 at a depth of 46.6 m in the SL section to correspond to the Miocene age. However, the
246 original studies of Zheng et al. (2000, 2001) cited by Ao et al. (2016, 2018) did not confirm
247 that the *Meriones* sp. belonged to the Miocene. Zheng et al., (2000, 2001) established that
248 another micromammal *Pseudomeriones* sp. existed in the Miocene, whereas the most
249 ancient *Meriones* representatives lived during the Pleistocene and the origin of ancestral
250 *Meriones* was set to the Pliocene (Chevret and Bobigny, 2005; Wang et al., 2013; Dianat
251 et al., 2017). Therefore the chronology presented in Anwar et al. (2015) and Zhang et al.
252 (2018, 2022) is consistent with the Pliocene-Pleistocene age for the SL section. We note
253 that the bottom of the SL red clay is not exposed in the outcrop and in the future it is
254 possible to reach the late Miocene red clay layers using drilling. The LL section is older
255 than the SL section considering the fossil evidence from both SL and LL that is supported
256 by the magnetostratigraphy.

257 The LL section is located in a valley with a lower elevation compared to the SL section
258 and has a ~ 400 m height difference with a 40 km horizontal separation of the sections
259 (Figure 1b). Taking it into account we combined both records that have overlapped each
260 other into a long magnetic susceptibility (LMS) record spanning from the Gauss chron to
261 C3A chron (Figure 7). Both MS records were stacked together by averaging the values
262 between two parts in the overlapping interval of 5.2 – 4 Ma. Figure 7 demonstrates
263 similarities of the general long-term trends between LMS and the JC section MS record

264 (Ding et al., 2001), while smaller-scale features differ in the terms of amplitudes.

265

266 **4. Discussion**

267 **4.1 Discovery of the 1.2 Myr cycle in the Asian monsoon record**

268 The typical changes of MS records in the eolian sediments of CLP are well known for their
269 close match with the global glacial-interglacial cycles depicted by the $\delta^{18}\text{O}$ records in
270 marine sediments and by the time-series of summer insolation at 65°N derived from orbital
271 solutions (Laskar et al., 2004). We obtained independent climate records from terrestrial
272 archives of CLP in order to reconstruct the atmospheric circulation in eastern Asia since
273 the late Miocene. We compared our stacked LMS record from the eastern part of CLP with
274 the inland JC red clay section (Figure 7a-d) (Ding et al., 2001).

275 The results of the wavelet analysis of the LMS record show a clear 405 kyr eccentricity
276 cycle between 7 and 2.5 Ma (Figure 7e) which is linked to the gravitational interaction of
277 Jupiter and Venus ($g_2 - g_5$), while the MS in the central CLP indicates an accentuation of
278 the 405 kyr band between 4 and 2.5 Ma (Figure 7f). Interestingly, a ~ 1.2 Myr grand cycle
279 of $s_4 - s_3$ obliquity modulation, linked to the orbital inclination rates of Mars and Earth,
280 is superimposed with the 405 and 100 kyr bands (Figure 7e & 7f) similarly to previous
281 climatic records (van Dam et al., 2006) and is interpreted as beats between secular
282 frequencies $p+s_4$ and $p+s_3$ (Laskar et al., 2004). The chaotic solar system has two major
283 secular resonances. The first argument, $\theta = (s_4 - s_3) - 2(g_4 - g_3)$ draws particular attention
284 because the two longest orbital secular frequencies, obliquity and precession modulations,

285 from $s_4 - s_3$ and $g_4 - g_3$ (~ 2.4 Myr) experienced intermittent chaotic transitions at $\sim 2:1$
286 resonance states, when ~ 1.2 Myr cycle dominates since 50 Ma (Hinnov, 2000; Laskar et
287 al., 2004; Palike et al., 2004; Crampton et al., 2018).

288 To further highlight the expression of the 405 and 100 kyr eccentricity bands within the
289 LMS and JS records, we applied a two-channel band-pass filter with 350–500 kyr and 80–
290 125 kyr bandwidths, respectively (red curves in Figure 8) after removing the long-term
291 trend that could be related to tectonic processes in the region (Anwar et al., 2015; R. Zhang,
292 Kravchinsky, et al., 2021; Zhang et al., 2022). The minima of each 405 kyr cycle after the
293 filter application between ~ 5.3 Ma and 2.5 Ma for both MS curves (Figure 8d & 8e)
294 correlate with the eccentricity maxima (Figure 8c). However, prior to this period, the
295 curves are out of phase suggesting that some other signal should have affected the climate
296 variations during the late Miocene. In contrast to the filtered signals and astronomical
297 cycles (red solid and green dashed lines), the unfiltered MS (Figure 8d, f) curves show less
298 variability but the conspicuous grand cycle related to the 1.2 Myr obliquity modulation is
299 evident between 7.1 and 4 Ma.

300

301 **4.2 Global documentation of the 1.2 Myr cycle that drives the Miocene-Pliocene** 302 **climate variations**

303

304 Obliquity, precession and their modulations have been shown to be important driving
305 forces of the global monsoon system which is sensitive to change in insolation, waxing
306 and waning of ice sheets and CO_2 concentration (Prell and Kutzbach, 1992; Nie et al.,

307 2008; Anwar et al., 2015; Nie, 2018; Zhang et al., 2022). Various time series, such as MS,
308 $\delta^{18}\text{O}$, SST and atmospheric CO_2 levels, display a significant climatic transition at ~ 5.3 Ma
309 (Beerling et al., 2011; Herbert et al., 2016; Holbourn et al., 2018; Tian et al., 2008; Liu et
310 al., 2019) (Figure 9). The MS records show that the intensification of the Tibetan Plateau
311 rise enhanced the 405 kyr band by a strengthened summer monsoon since $\sim 3.6 - 4.2$ Ma
312 (Figure 9b, c) (Nie et al., 2008). Therefore, we argue that tectonic processes that impacted
313 regional land-sea heat exchanges strongly influence the orbital-sensitive climate
314 fluctuations, which, in turn, induced significant changes in the insolation-forced summer
315 monsoon and led to introducing the tectonic related long-term trend towards two-three
316 times higher values of MS in the interval between ~ 4.2 and 3.6 Ma (Figure 9b, c). In the
317 ocean, the negative shifts of benthic $\delta^{18}\text{O}$ records (Figure 9d) correspond to the increase
318 of MS (Figure 9b, c) that is consistent with a dominant summer monsoon regime linked to
319 global warming at 5.3 Ma (Holbourn et al., 2018). In contrast, the positive shifts of $\delta^{18}\text{O}$
320 (Figure 9d) and the decrease of MS (Figure 9b, c) and SST (Figure 9h) correspond to a
321 global cooling and inland aridification that led to the birth of the Sahara and Taklimakan
322 deserts ~ 7 Ma (Schuster et al., 2006; Sun et al., 2009).

323 Previous studies have pointed out that a strengthened winter monsoon during the 7.1–5.5
324 Ma time interval was associated with an expansion of ice sheets in the Northern
325 Hemisphere (Wolf-Welling et al., 1996; Thiede et al., 1998; Holbourn et al.; 2018) and
326 indicated a global cooling during the Late Miocene (Zachos et al., 2001). The $\delta^{18}\text{O}$ record
327 of benthic foraminifera showed a clear decrease indicating a warming transition $\sim 5.5 - 5.3$
328 Ma. (Holbourn et al.; 2018; Westerhold et al., 2020). Such interpretation of both climatic
329 variations at ~ 7 and 5.3 Ma is supported by the variability of the 1.2 Ma obliquity

330 modulation (Figure 9a & Figure 10) during the 7.6 – 3.6 Ma intervals. The grand obliquity
331 curve is on the descent at 7 Ma and on the rise at 5.3 Ma. Several lines of evidence indicate
332 that the closure of the Panama and Indonesia seaways may have also caused a significant
333 reorganization of ocean circulation and increased the Gulf Stream yielding substantial
334 transfer of warm and saline water masses to high northern latitudes during the Miocene-
335 Pliocene between 6 and 2.7 Ma (Cane et al., 2001; Haug et al., 2001). The warm conditions
336 at high latitudes (Figure 9f) may result from the massive input of warmer water. The
337 planktonic foraminifera isotopic records from the Caribbean Sea indicate that salinity of
338 the Caribbean surface waters already started to increase at the beginning of Pliocene,
339 suggesting a weakened surface water circulation between the tropical Atlantic and Pacific
340 Oceans as a result of the growth of the Central American isthmus of Panama (Haug et al.,
341 1998). It probably led to a climate pattern of a 405-kyr cycle in the Western Hemisphere
342 even earlier than the Asian Monsoon region (Figure 9g) (Nie, 2018). However, there is
343 still controversy, to determine when the seaway closed, if not possible, until the “Great
344 American Exchange” of Vertebrates between North and South America that occurred ~
345 2.7 – 2.6 Ma (Molnar, 2008). On the other hand, the thickening of the equatorial Western
346 Pacific warm pool triggered by the closure of the Panama and Indonesian seaways may
347 have expanded the exchanges of heat and moisture toward high latitudes. This process
348 contributed to the warming up of the South China Sea water and to increase the
349 precipitation on the Asian continent (Yan et al., 1992; Li et al., 2008). The gradual growth
350 of the Tibetan Plateau ~ 4.2 Ma may have also increased the air pressure gradient between
351 land and sea, resulting in greater seasonal precipitation within the monsoon influence
352 region. The 1.2 and 0.405 Myr long amplitude modulations of the obliquity and precession

353 cycles are prominent features of the climate pattern between the late Miocene and
354 Pliocene, especially for the Asian monsoon.

355

356 **5. Conclusions**

357 Our interpretation of the LMS record shows that the Asian summer monsoon appears to
358 be orbitally controlled by the 1.2 Myr grand obliquity cycle band between 7.7 and 4 Ma
359 and by the 0.405 Myr long eccentricity band between 4 and 2.5 Ma. We conclude that
360 global cooling and warming that occurred 7 and 5.3 Ma respectively, as well as the
361 Antarctic ice volume, carbon cycle dynamics and the monsoon forcing of the upper-ocean
362 circulation were all triggered by the grand obliquity variations before the middle Pliocene.
363 Since then, a series of major tectonic events such as the closure of the Panama and
364 Indonesian seaways and the uplift of the Tibetan Plateau, accelerated the transition from a
365 1.2 Myr obliquity-dominated to a 0.405 Myr eccentricity-dominated climate variability for
366 the Asian monsoon.

367

368 **Conflict of Interest**

369 The authors declare no conflicts of interest relevant to this study.

370

371 **Data Availability Statement**

372 The data are available at <https://doi.org/10.5281/zenodo.6391476>

373

374 **Acknowledgments**

375 This study was funded by the National Natural Science Foundation of China (41772027,
376 41972035 and 41950410574) for R.Z., J.Q. and J.L., the China Scholarship Council for
377 J.Q., and the Natural Sciences and Engineering Research Council of Canada (NSERC
378 grant RGPIN-2019-04780) for V.A.K. The authors thank two anonymous reviewers and
379 an associate editor for their valuable comments that helped to substantially improve the
380 manuscript. Rui Zhang and Vadim A. Kravchinsky prepared the manuscript with
381 intellectual contributions from all authors.

382

383

384 **References**

- 385 An, Z., Kutzbach, J.E., Prell, W.L., Porter, S.C., 2001. Evolution of Asian monsoons and phased uplift of
386 the Himalaya–Tibetan plateau since Late Miocene times. *nature* 411, 62–66.
- 387 Anwar, T., Kravchinsky, V.A., Zhang, R., 2015. Magneto- and cyclostratigraphy in the red clay sequence:
388 New age model and paleoclimatic implication for the eastern Chinese Loess Plateau. *Journal of*
389 *Geophysical Research: Solid Earth*, 120, 6758–6770.
- 390 Ao, H., Roberts, A.P., Dekkers, M.J., Liu, X., Rohling, E.J., Shi, Z., An, Z., Zhao, X., 2016. Late Miocene–
391 Pliocene Asian monsoon intensification linked to Antarctic ice-sheet growth. *Earth and Planetary*
392 *Science Letters* 444, 75–87.
- 393 Badgley, C., Barry, J.C., Morgan, M.E., Nelson, S.V., Behrensmeyer, A.K., Cerling, T.E., Pilbeam, D., 2008.
394 Ecological changes in Miocene mammalian record show impact of prolonged climatic forcing.
395 *Proceedings of the National Academy of Sciences*, 105, 12145–12149.
- 396 Beerling, D.J., Royer, D.L., 2011. Convergent Cenozoic CO₂ history. *Nature Geoscience* 4, 418–420.
- 397 Bolton, C.T., Stoll, H.M., 2013. Late Miocene threshold response of marine algae to carbon dioxide
398 limitation. *Nature* 500, 558–562.

- 399 Boos, W.R., Kuang, Z., 2010. Dominant control of the South Asian monsoon by orographic insulation versus
400 plateau heating. *Nature* 463, 218–222.
- 401 Burke, K.D., Williams, J.W., Chandler, M.A., Haywood, A.M., Lunt, D.J., Otto-Bliesner, B.L., 2018.
402 Pliocene and Eocene provide best analogs for near-future climates. *Proceedings of the National*
403 *Academy of Sciences*, 115, 13288–13293.
- 404 Cane, M.A., Molnar, P., 2001. Closing of the Indonesian seaway as a precursor to east African aridification
405 around 3–4 million years ago. *Nature* 411, 157–162.
- 406 Cerling, T.E., Harris, J.M., MacFadden, B.J., Leakey, M.G., Quade, J., Eisenmann, V., Ehleringer, J.R.,
407 1997. Global vegetation change through the Miocene/Pliocene boundary. *Nature* 389, 153–158.
- 408 Chevret, P. and Bobigny, G., 2005. Systematics and evolution of the subfamily Gerbillinae (Mammalia,
409 Rodentia, Muridae). *Molecular Phylogenetics and Evolution* 35, 674–688.
- 410 Crampton, J.S., Meyers, S.R., Cooper, R.A., Sadler, P.M., Foote, M., Harte, D., 2018. Pacing of Paleozoic
411 macroevolutionary rates by Milankovitch grand cycles. *Proceedings of the National Academy of*
412 *Sciences* 115, 5686–5691.
- 413
- 414 Dianat, M., Darvish, J., Cornette, R., Aliabadian, M., Niolas, V., 2017. Evolutionary history of the Persian
415 Jird, *Meriones persicus*, based on genetics, species distribution modelling and morphometric data.
416 *Journal of Zoological Systematics & Evolutionary Research*, 55, 29–45.
- 417 Ding, Z., Yang, S., Hou, S., Wang, X., Chen, Z., Liu, T., 2001. Magnetostratigraphy and sedimentology of
418 the Jingchuan red clay section and correlation of the Tertiary eolian red clay sediments of the Chinese
419 Loess Plateau. *Journal of Geophysical Research: Solid Earth*, 106, 6399–6407.
- 420 Dowsett, H.J., Chandler, M.A., Cronin, T.M. and Dwyer, G.S. Middle Pliocene sea surface temperature
421 variability. *Paleoceanography*, 20, PA2014 (2005).
- 422 Fedorov, A.V., Dekens, P.S., McCarthy, M., Ravelo, A.C., deMenocal, P.B., Barreiro, M., Pacanowski,
423 R.C., Philander, S.G., 2006. The Pliocene Paradox (Mechanisms for a Permanent El Niño). *Science*
424 312, 1485–1489.
- 425 Hao, Q., Wang, L., Oldfield, F., Peng, S., Qin, L., Song, Y., Xu, B., Qiao, Y., Bloemendal, J., Guo, Z., 2012.
426 Delayed build-up of Arctic ice sheets during 400,000-year minima in insolation variability. *Nature*
427 490, 393–396.
- 428 Haug, G.H., Tiedemann, R., 1998. Effect of the formation of the Isthmus of Panama on Atlantic Ocean
429 thermohaline circulation. *Nature* 393, 673–676.
- 430 Haug, G.H., Tiedemann, R., Zahn, R., Ravelo, A.C., 2001. Role of Panama uplift on oceanic freshwater
431 balance. *Geology*, 29, 207–210.
- 432 Herbert, T.D., Lawrence, K.T., Tzanova, A., Peterson, L.C., Caballero-Gill, R., Kelly, C.S., 2016. Late
433 Miocene global cooling and the rise of modern ecosystems. *Nature Geoscience* 9, 843–847.
- 434 Hinnov, L.A., 2000. New perspectives on orbitally forced stratigraphy. *Annual Review of Earth and*
435 *Planetary Sciences* 28, 419–475.
- 436 Holbourn, A.E., Kuhnt, W., Clemens, S.C., Kochhann, K.G., Jöhnck, J., Lübbers, J., Andersen, N., 2018.
437 Late Miocene climate cooling and intensification of southeast Asian winter monsoon. *Nature*
438 *Communications* 9, 1584.
- 439 Huang, Y., Clemens, S.C., Liu, W., Wang, Y., Prell, W.L., 2007. Large-scale hydrological change drove the
440 late Miocene C4 plant expansion in the Himalayan foreland and Arabian Peninsula. *Geology* 35, 531–
441 534.

- 442 LaRiviere, J.P., Ravelo, A.C., Crimmins, A., Dekens, P.S., Ford, H.L., Lyle, M., Wara, M.W., 2012. Late
443 Miocene decoupling of oceanic warmth and atmospheric carbon dioxide forcing. *Nature* 486, 97–100.
- 444 Laskar, J., Correia, A.C.M., Gastineau, M., Joutel, F., Levrard, B., Robutel, P., 2004. Long term evolution
445 and chaotic diffusion of the insolation quantities of Mars. *Icarus*, 170, 343–364.
- 446 Laskar, J., Joutel, F., Boudin, F., 1993. Orbital, precessional, and insolation quantities for the Earth from -
447 20 Myr to +10 Myr. *Astronomy and Astrophysics*, 270, 522–533.
- 448 Lawrence, K.T., Liu, Z., Herbert, T.D., 2006. Evolution of the Eastern Tropical Pacific Through Plio-
449 Pleistocene Glaciation. *Science* 312, 79–83.
- 450 Lewis, A.R., Marchant, D.R., Ashworth, A.C., Hedenäs, L., Hemming, S.R., Johnson, J.V., Leng, M.J.,
451 Machlus, M.L., Newton, A.E., Raine, J.I., Willenbring, J.K., 2008. Mid-Miocene cooling and the
452 extinction of tundra in continental Antarctica. *Proceedings of the National Academy of Sciences* 105,
453 10676–10680.
- 454 Li, F., Rousseau, D.D., Wu, N., Hao, Q., Pei, Y., 2008. Late Neogene evolution of the East Asian monsoon
455 revealed by terrestrial mollusk record in Western Chinese Loess Plateau: from winter to summer
456 dominated sub-regime. *Earth Planet. Sci. Lett.* 274, 439–447.
- 457 Liu, J., Tian, J., Liu, Z., Herbert, T.D., Fedorov, A.V., Lyle, M., 2019. Eastern equatorial Pacific cold tongue
458 evolution since the late Miocene linked to extratropical climate. *Science advances* 5, eaau6060.
- 459 Naish, T., Powell, R., Levy, R., Wilson, G., Scherer, R., Talarico, F., Krissek, L., Niessen, F., Pompilio,
460 M., Wilson, T., Carter, L., 2009. Obliquity-paced Pliocene West Antarctic ice sheet oscillations.
461 *Nature* 458, 322–329.
- 462 Nie, J., King, J.W., Fang, X., 2008. Tibetan uplift intensified the 400 ky signal in paleoclimate records at 4
463 Ma. *Geological Society of America Bulletin* 120, 1338–1344.
- 464 Nie, J. 2018. The Plio-Pleistocene 405-kyr climate cycles. *Palaeogeography, palaeoclimatology,*
465 *palaeoecology* 510, 26–30.
- 466 Ogg, J. G., 2012. Geomagnetic Polarity Time Scale. In F. M. Gradstein, J. G. Ogg, M. D. Schmitz, & G. M.
467 Ogg (Eds.), *The Geologic Time Scale 2012*. Amsterdam: Elsevier, (pp. 85–113).
- 468 Prell, W.L., Kutzbach, J.E., 1992. Sensitivity of the Indian monsoon to forcing parameters and implications
469 for its evolution. *Nature* 360, 647–652.
- 470 Ravelo, A.C., Andreasen, D.H., Lyle, M., Lyle, A.O., Wara, M.W., 2004. Regional climate shifts caused by
471 gradual global cooling in the Pliocene epoch. *Nature* 429, 263–267.
- 472 Schuster, M., Düringer, P., Ghienne, J.F., Vignaud, P., Mackaye, H.T., Likius, A., 2006. Brunet, M. The age
473 of the Sahara Desert. *Science* 311, 821.
- 474 Sun, J., Zhang, Z., Zhang, L., 2009. New evidence on the age of the Taklimakan Desert. *Geology* 37, 159–
475 162.
- 476 Sun, Y., Yin, Q., Crucifix, M., Clemens, S.C., Araya-Melo, P., Liu, W., Qiang, X., Liu, Q., Zhao, H., Liang,
477 L., Chen, H., 2019. Diverse manifestations of the mid-Pleistocene climate transition. *Nature*
478 *communications*, 10, 352.
- 479 Thiede, J., Winkler, A., Wolf-Welling, T., Eldholm, O., Myhre, A.M., Baumann, K.H., Henrich, R., Stein,
480 R., 1998. Late Cenozoic history of the Polar North Atlantic: results from ocean drilling. *Quaternary*
481 *Science Reviews*, 17, 185–208.
- 482 van Dam, J., Abdul Aziz, H., Alvarez Sierra, M.A., Hilgen, F.J., van den Hoek Ostende L.W., Lourens, L.J.,
483 Mein, P., van der Meulen, A.J., Pelaez-Campomanes, P., 2006. Long-period astronomical forcing of
484 mammal turnover. *Nature* 443, 687–691.

- 485 Wang, Y., Zhao, L., Fang, F., Liao, J., Liu N., 2013. Intraspecific molecular phylogeny and phylogeography
486 of the *Meriones meridianus* (Rodentia: Cricetidae) complex in northern China reflect the processes of
487 desertification and the Tianshan Mountains uplift. *Biological Journal of the Linnean Society* 110, 362–
488 383.
- 489 Westerhold, T., Marwan, N., Drury, A.J., Liebrand, D., Agnini, C., Anagnostou, E., Barnet, J.S., Bohaty,
490 S.M., De Vleeschouwer, D., Florindo, F., Frederichs, T., 2020. An astronomically dated record of
491 Earth's climate and its predictability over the last 66 million years. *Science*, 369, 1383–1387.
- 492 Wolf-Welling, T.C., Cremer, M., O'Connell, S., Winkler, A., Thiede, J., 1996. Cenozoic Arctic gateway
493 paleoclimate variability: Indications from changes in coarse-fraction composition. *Proceedings of the*
494 *Ocean Drilling Program, Scientific Results* 151, 515–568.
- 495 Xu, Y., Yue, L., Li, J., Sun, L., Sun, B., Zhang, J., Ma, J., Wang, J., 2009. An 11-Ma-old red clay sequence
496 on the Eastern Chinese Loess Plateau. *Palaeogeography, Palaeoclimatology, Palaeoecology* 284, 383–
497 391.
- 498 Xu, Y., Yue, L., Li, J., Wang, J., Sun, B., Sun, L., Zhang, J., Ma, J., 2013. Late Neogene red clay in the
499 Fuxing area of western foothills of the Lüliang Mountain. *Journal of Stratigraphy*, 37, 33–40 (in
500 Chinese).
- 501 Yan, X., Ho, C., Zheng, Q. and Klemas, V., 1992. Temperature and size variabilities of the west Pacific
502 warm pool. *Science* 258, 1643–1645.
- 503 Zachos, J., Pagani, M., Sloan, L., Thomas, E., Billups, K., 2001. Trends, rhythms, and aberrations in global
504 climate 65 Ma to present. *science* 292, 686–693.
- 505 Zheng, S., Zhang, Z., 2000. Late Miocene-Early Pleistocene micromammals from Wenwanggou of Lingtai,
506 Gansu, China. *Vertebrata Palasiatica*, 38, 58–71.
- 507 Zheng, S., Zhang, Z., 2001. Late Miocene-early Pleistocene biogeography of the Leijiahe area, Lingtai,
508 Gansu. *Vertebrata Palasiatica* 39, 215–228 (in Chinese).
- 509 Zhang, R., Kravchinsky, V. A., Anwar, T., Yue, L., Li, J., Jiao, J., 2018. Comment on "Late Miocene-
510 Pliocene Asian monsoon intensification linked to Antarctic ice-sheet growth" [*Earth Planet. Sci. Lett.*
511 444 (2016) 75-87]. *Earth and Planetary Science Letters* 503, 248–251.
- 512 Zhang, R., Kravchinsky, V. A., Qin, J., Goguitchaichvili, A., Li, J., 2021. One and a Half Million Yearlong
513 Aridity During the Middle Eocene in North-West China Linked to a Global Cooling Episode. *Journal*
514 *of Geophysical Research: Solid Earth* 126, e2020JB021037.
- 515 Zhang, R., Wei, X., Kravchinsky, V. A., Yue, L., Zheng, Y., Qin, J., Yang, L., Ma, M., Xian, F., Gong, H.,
516 Zhang, Y., Liu, X., 2021. "Tiny wiggles" in the late Miocene red clay deposits in the north-east of the
517 Tibetan Plateau. *Geophysical Research Letters*, 48, e2021GL093962.
- 518 Zhang, R., Li, X., Xu, Y., Li, J., Sun, L., Yue, L., Pan, F., Xian, F., Wei, X., Cao, Y., 2022. The 173-kyr
519 obliquity cycle pacing the Asian monsoon in the eastern Chinese Loess Plateau from late Miocene to
520 Pliocene. *Geophysical Research Letters*, 49, e2021GL097008.
- 521 Zhu, Y., Zhou, L., Mo, D., Kaakinen, A., Zhang, Z. and Fortelius, M., 2008. A new magnetostratigraphic
522 framework for late Neogene Hipparion Red Clay in the eastern Loess Plateau of China.
523 *Palaeogeography, Palaeoclimatology, Palaeoecology* 268, 47–57.

524

525 **References from Supporting Information**

- 526 An, Z., 2000. The history and variability of the East Asian paleomonsoon climate. *Quaternary Science*
527 *Reviews* 19, 171–187.

- 528 An, Z., Kukla, G., Porter, S. C., Xiao, J., 1991a. Late Quaternary dust flow on the Chinese loess plateau.
529 *Catena* 18, 125–132.
- 530 An, Z., Kukla, G., Porter, S. C., Xiao, J., 1991b. Magnetic susceptibility evidence of monsoon variation on
531 the Loess Plateau of central China during the last 130,000 years. *Quaternary Research* 36, 29–36.
- 532 An, Z., Kutzbach, J. E., Prell, W. L., Porter, S. C., 2001. Evolution of Asian monsoons and phased uplift of
533 the Himalaya–Tibetan plateau since Late Miocene times. *nature* 411, 62–66.
- 534 Anwar, T., Kravchinsky, V. A., Zhang, R., 2015. Magneto- and cyclostratigraphy in the red clay sequence:
535 New age model and paleoclimatic implication for the eastern Chinese Loess Plateau. *Journal of*
536 *Geophysical Research: Solid Earth* 120, 6758–6770.
- 537 Ao, H., Roberts, A. P., Dekkers, M. J., Liu, X., Rohling, E. J., Shi, Z., An, Z. and Zhao, X., 2016. Late
538 Miocene–Pliocene Asian monsoon intensification linked to Antarctic ice-sheet growth. *Earth and*
539 *Planetary Science Letters* 444, 75–87.
- 540 Ao, H., Roberts, A. P., Dekkers, M. J., Liu, X., Rohling, E. J., Shi, Z., An, Z., Chang, H., Qiang, X. and
541 Zhao, X., 2018. Reply to Zhang et al.: Late Miocene–Pliocene magnetostratigraphy of the Shilou Red
542 Clay on the eastern Chinese Loess Plateau. *Earth and Planetary Science Letters*, 503, 252–255.
- 543 Ding, Z., Rutter, N., Han, J., Liu, T., 1992. A coupled environmental system formed at about 2.5 Ma in east-
544 Asia. *Palaeogeography, Palaeoclimatology, Palaeoecology* 94, 223–242.
- 545 Ding, Z., Sun, J., Yang, S., Liu, T., 1998a. Preliminary magnetostratigraphy of a thick eolian red clay-loess
546 sequence at Lingtai, the Chinese Loess Plateau. *Geophysical Research Letters* 25, 1225–1228.
- 547 Ding, Z., Sun, J., Liu, T., Zhu, R., Yang, S. and Guo, B., 1998b. Wind-blown origin of the Pliocene red clay
548 formation in the central Loess Plateau, China. *Earth and Planetary Science Letters* 161, 135–143.
- 549 Ding, Z., Xiong, S., Sun, J., Yang, S., Gu, Z. and Liu, T., 1999. Pedostratigraphy and paleomagnetism of a
550 ~7.0 Ma eolian loess-red clay sequence at Lingtai, Loess Plateau, north-central China and the
551 implications for paleomonsoon evolution. *Palaeogeography, Palaeoclimatology, Palaeoecology* 152,
552 49–66.
- 553 Ding, Z., Yang, S., Hou, S., Wang, X., Chen, Z. and Liu, T., 2001. Magnetostratigraphy and sedimentology
554 of the Jingchuan red clay section and correlation of the Tertiary eolian red clay sediments of the Chinese
555 Loess Plateau. *Journal of Geophysical Research: Solid Earth* 106, 6399–6407.
- 556 Evans, M. E., Wang, Y., Rutter, N., Ding, Z., 1991. Preliminary magnetostratigraphy of the red clay
557 underlying the loess sequence at Baoji, China. *Geophysical Research Letters* 18, 1409–1412.
- 558 Guo, Z., Ruddiman, W. F., Hao, Q., Wu, H., Qiao, Y., Zhu, R., Peng, S., Wei, J., Yuan, B. and Liu, T., 2002.
559 Onset of Asian desertification by 22 Myr ago inferred from loess deposits in China. *Nature* 416, 159–
560 163.
- 561 Hao, Q., Guo, Z., 2004. Magnetostratigraphy of a late Miocene–Pliocene loess-soil sequence in the western
562 Loess Plateau in China. *Geophysical Research Letters* 31.
- 563 Heller, F., Liu, T., 1982. Magnetostratigraphical dating of loess deposits in China. *Nature* 300, 431–433.
- 564 Kukla, G., An, Z., 1989. Loess Stratigraphy in Central China. *Palaeogeography Palaeoclimatology*
565 *Palaeoecology* 72, 203–225.
- 566 Laskar, J., Correia, A.C.M., Gastineau, M., Joutel, F., Levrard, B., Robutel, P., 2004. Long term evolution
567 and chaotic diffusion of the insolation quantities of Mars. *Icarus*, 170, 343–364.
- 568 Li, F., Rousseau, D. D., Wu, N., Hao, Q., Pei, Y., 2008. Late Neogene evolution of the East Asian monsoon
569 revealed by terrestrial mollusk record in Western Chinese Loess Plateau: from winter to summer
570 dominated sub-regime. *Earth and Planetary Science Letters* 274, 439–447.

- 571 Lisiecki, L. E., Lisiecki, P. A., 2002. Application of dynamic programming to the correlation of paleoclimate
572 records. *Paleoceanography*, 17, 1–1.
- 573 Lisiecki, L. E., Raymo, M. E., 2005. A Pliocene-Pleistocene stack of 57 globally distributed benthic $\delta^{18}\text{O}$
574 records. *Paleoceanography*, 20.
- 575 Liu, T., (1985), Loess and Environment, pp. 31–67, China Ocean Press, Beijing.
- 576 Ogg, J. G. Geomagnetic Polarity Time Scale. In F. M. Gradstein, J. G. Ogg, M. D. Schmitz, & G. M. Ogg
577 (Eds.), The Geologic Time Scale 2012. Amsterdam: Elsevier (pp. 85-113) (2012).
- 578 Qiang, X., An, Z., Song, Y., Chang, H., Sun, Y., Liu, W., Ao, H., Dong, J., Fu, C., Wu, F. and Lu, F., 2011.
579 New eolian red clay sequence on the western Chinese Loess Plateau linked to onset of Asian
580 desertification about 25 Ma ago. *Science China Earth Sciences* 54, 136–144.
- 581 Qiang, X., Li, Z., Powell, C. M., Zheng, H., 2001. Magnetostratigraphic record of the Late Miocene onset
582 of the East Asian monsoon, and Pliocene uplift of northern Tibet. *Earth and Planetary Science Letters*,
583 187, 83–93.
- 584 Rutter, N., Ding, Z., Evans, M. E., Liu, T., 1991. Baoji-type pedostratigraphic section, Loess Plateau, north-
585 central China. *Quaternary Science Reviews* 10, 1–22.
- 586 Song, Y., Fang, X., Torii, M., Ishikawa, N., Li, J. and An, Z., 2007. Late Neogene rock magnetic record of
587 climatic variation from Chinese eolian sediments related to uplift of the Tibetan Plateau. *Journal of*
588 *Asian Earth Sciences* 30, 324–332.
- 589 Song, Y., Fang, X., Chen, X., Torii, M., Ishikawa, N., Zhang, M., Yang, S. and Chang,., 2018. Rock magnetic
590 record of late Neogene red clay sediments from the Chinese Loess Plateau and its implications for East
591 Asian monsoon evolution. *Palaeogeography, Palaeoclimatology, Palaeoecology* 510, 109–123.
- 592 Sun, D., An, Z., Shaw, J., Bloemendal, J., Sun, Y., 1998b. Magnetostratigraphy and palaeoclimatic
593 significance of Late Tertiary aeolian sequences in the Chinese Loess Plateau. *Geophysical Journal*
594 *International* 134, 207–212.
- 595 Sun, D., John, S., An, Z., Cheng, M., Yue, L., 1998a. Magnetostratigraphy and paleoclimatic interpretation
596 of a continuous 7.2 Ma Late Cenozoic eolian sediments from the Chinese Loess Plateau. *Geophysical*
597 *Research Letters* 25, 85–88.
- 598 Sun, Y., An, Z., Clemens, S. C., Bloemendal, J., Vandenberghe, J., 2010. Seven million years of wind and
599 precipitation variability on the Chinese Loess Plateau. *Earth and Planetary Science Letters* 297, 525–
600 535.
- 601 Torrence, C. and Compo, G.P., 1998. A practical guide to wavelet analysis. *Bulletin of the American*
602 *Meteorological Society* 79, 61-78.
- 603 Xu, Y., Yue, L., Li, J., Sun, L., Sun, B., Zhang, J., Ma, J. and Wang, J., 2009. An 11-Ma-old red clay
604 sequence on the Eastern Chinese Loess Plateau. *Palaeogeography, Palaeoclimatology, Palaeoecology*
605 284, 383–391.
- 606 Zhang, R., Kravchinsky, V. A., Anwar, T., Yue, L., Li, J. and Jiao, J., 2018. Comment on "Late Miocene-
607 Pliocene Asian monsoon intensification linked to Antarctic ice-sheet growth"[*Earth Planet. Sci. Lett.*
608 444 (2016) 75-87]. *Earth and Planetary Science Letters* 503, 248–251.
- 609 Zhang, R., Kravchinsky, V. A., Qin, J., Goguitchaichvili, A., Li, J., 2021a. One and a Half Million Yearlong
610 Aridity During the Middle Eocene in North-West China Linked to a Global Cooling Episode. *Journal*
611 *of Geophysical Research: Solid Earth* 126, e2020JB021037.
- 612 Zhang, R., Wei, X., Kravchinsky, V. A., Yue, L., Zheng, Y., Qin, J., Yang, L., Ma, M., Xian, F., Gong, H.,
613 Zhang, Y., Liu, X., 2021b. "Tiny wiggles" in the late Miocene red clay deposits in the north-east of the
614 Tibetan Plateau. *Geophysical Research Letters*, 48, e2021GL093962.

- 615 Zhang, R., Li, X., Xu, Y., Li, J., Sun, L., Yue, L., Pan, F., Xian, F., Wei, X., Cao, Y., 2022. The 173-kyr
616 obliquity cycle pacing the Asian monsoon in the eastern Chinese Loess Plateau from late Miocene to
617 Pliocene. *Geophysical Research Letters*, 49, e2021GL097008.
- 618 Zheng, H., An, Z., Shaw, J., 1992. New contributions to Chinese Plio-pleistocene magnetostratigraphy.
619 *Physics of the Earth and Planetary Interiors*, 70, 146–153.
- 620 Zhu, Y., Zhou, L., Mo, D., Kaakinen, A., Zhang, Z. and Fortelius, M., 2008. A new magnetostratigraphic
621 framework for late Neogene Hipparion Red Clay in the eastern Loess Plateau of China.
622 *Palaeogeography, Palaeoclimatology, Palaeoecology* 268, 47–57.
- 623
- 624

625 **Figure Captions**

626 **Figure 1.** (a) Topographic map of the present-day Chinese Loess Plateau with studied
627 locations (yellow star and yellow dots). Liulin (yellow star); SL- Shilou, JC- Jingchuan.
628 (b) Map showing the location of LL (green triangle) and SL (red star) red clay sections
629 and the surrounding main rivers. Red dashed lines represent the contours and the elevation
630 is in meters.

631

632 **Figure 2.** χ -T curves for selected samples from the Liulin red clay sequence. The red and
633 blue lines represent heating and cooling curves, respectively.

634

635 **Figure 3.** Representative thermal demagnetization curves for different depths.

636

637 **Figure 4.** Lithostratigraphy, inclination, declination and VGP as a function of depth, and
638 the magnetic polarity interpretation of the Liulin red clay section, together with a
639 correlation to the geomagnetic timescale (Ogg, 2012). Red dots show the measuring
640 samples. Legend: 1—red clay with strong pedogenesis, 2—sandy red clay, 3—red clay
641 with weak pedogenesis, 4—carbonate layer, 5—mudstone, 6—fossil, 7—sandstone, 8—
642 gravel, 9—carbonate nodules.

643

644 **Figure 5.** Wavelet analysis of the magnetic susceptibility signal before (a) and after tuning
645 (b), the coarse fraction ($>63\mu\text{m}$) content before (c) and after tuning (d). Magnetic

646 susceptibility and Grain size was detrended with the Lowess smoothing method. The red
647 line is the two-band-filter signal with bandwidths of 350–500 kyr and 80–125 kyr. The
648 green solid line shows the long trend of MS (a,b)and GS (c,d) signals. The purple dashed
649 line marks the orbital period. The thin black contour encloses regions of greater than 95%
650 confidence for a red-noise process with a lag coefficient of 0.8. The thick black contour
651 indicates the cone of influence. The global wavelet spectrum to the right illustrates the
652 mean red noise spectrum, as indicated by the green dashed line. The color bars correspond
653 to wavelet power.

654

655 **Figure 6.** Sedimentation rates are determined on the basis of the magnetostratigraphic
656 correlations. Black dashed lines denote the typical sedimentation rate range for the red
657 clay of the CLP (Zhang et al., 2018). The red dashed line represents the average
658 sedimentation rate of the Liulin section determined by the magnetostratigraphy.

659

660 **Figure 7.** Comparison of magnetic susceptibility as a function of age from red clay
661 sections in the Chinese Loess Plateau. Three stages of different climate conditions as
662 shown by the MS. (a) MS of the LL red clay section. (b) MS of the SL red clay section
663 (Anwar et al., 2015). (c) LMS of the combined LL and SL red clay sections. (d) MS of the
664 JC red clay section (Ding et al., 2001). (e)Wavelet analysis of magnetic susceptibility
665 records from the LMS. (f) Wavelet spectrum of magnetic susceptibility from the JC
666 section.

667

668 **Figure 8.** Milankovitch cycles between 7.8 and 2.5 Ma were derived from the astronomical
669 solution (Laskar et al., 2004) and the Asian monsoon record. a. Amplitude modulation of
670 the precession solution (blue line) with its envelope curve (black dashed line) with the
671 $\sim 100,000$ and $\sim 405,000$ cycles. b. The ~ 1.2 Myr amplitude modulation (green line) of the
672 obliquity solution (Laskar et al., 2004) (blue line). c. Eccentricity solution (Laskar et al.,
673 2004). d. Long magnetic susceptibility (LMS) is detrended by the Lowess smoothing
674 method (blue). e Magnetic susceptibility from JC section after detrending using the
675 Lowess smoothing method (blue) (Ding et al., 2001). Red lines indicate the two-band filter
676 with bandwidths of 350–500 kyr and 80–125 kyr in d,e.

677

678 **Figure 9.** Compilation of Asian monsoon and global climatic proxies. a. Illustration of the
679 eccentricity solution (Laskar et al., 2004) (blue solid and dashed lines) and the ~ 1.2 Myr
680 grand cycles/obliquity modulation (red solid and dashed line). b. Combined LMS record
681 of the LL and SL sections. c. MS from JC section in the central CLP (Ding et al., 2001).
682 d. Benthic $\delta^{18}\text{O}$ global record (Westerhold et al., 2020) (blue) and benthic $\delta^{18}\text{O}$ record
683 from ODP Site 1148 (Tian et al., 2008) (red) and $\delta^{18}\text{O}$ from ODP Site 999 (Haug and
684 Tiedemann, 1998). e. Stacked SST from mid-high (pink) and tropical (brown) latitudes.
685 Pacific mid-high latitude records are integrated from DSDP Site 594, ODP Sites 883/884,
686 887, 1010, 1012, 1021, 1125 and 1208; Pacific tropical records are integrated from the
687 IODP Sites U1337, U1338, ODP Sites 846, 847, 850 and 1241 (Liu et al., 2019). f.
688 Atmospheric CO_2 history during the past 8 Myr from different proxies (Beerling et al.,
689 2011; Herbert et al., 2016). The horizontal red line indicates the Northern Hemisphere
690 glaciation threshold (approx. 280 ppm). g. $\delta^{13}\text{C}$ record (yellow) and carbonate sand-

691 fraction mass accumulation rates (purple) from ODP site 999 (Haug et al., 1998).

692

693 **Figure 10.** The simplified climate mode for Asian monsoon from late Miocene to
694 Pliocene. a. Eccentricity solution (Laskar et al., 2004) (blue solid and dashed lines), and
695 the ~1.2 Myr obliquity modulation (green solid line from 8 to 4 Ma and green dashed line
696 from 4 to 2.5 Ma). b. Mathematical model showing the 1.2 Myr grand cycles (red) during
697 the 8 to 4 Ma ($Y1 = \cos(2 \times \pi \times (1/1200) \times t)$); the 400 eccentricity cycles (blue) ($Y2 = \sin$
698 $(2 \times \pi \times (1/400) \times t)$) and the stepped tectonics (green arrow) ($Y3$) during the 4 to 2.5 Ma;
699 compound of long eccentricity and stepped tectonics (yellow) ($Y4 = Y2 \times Y3$).

Figure 1.

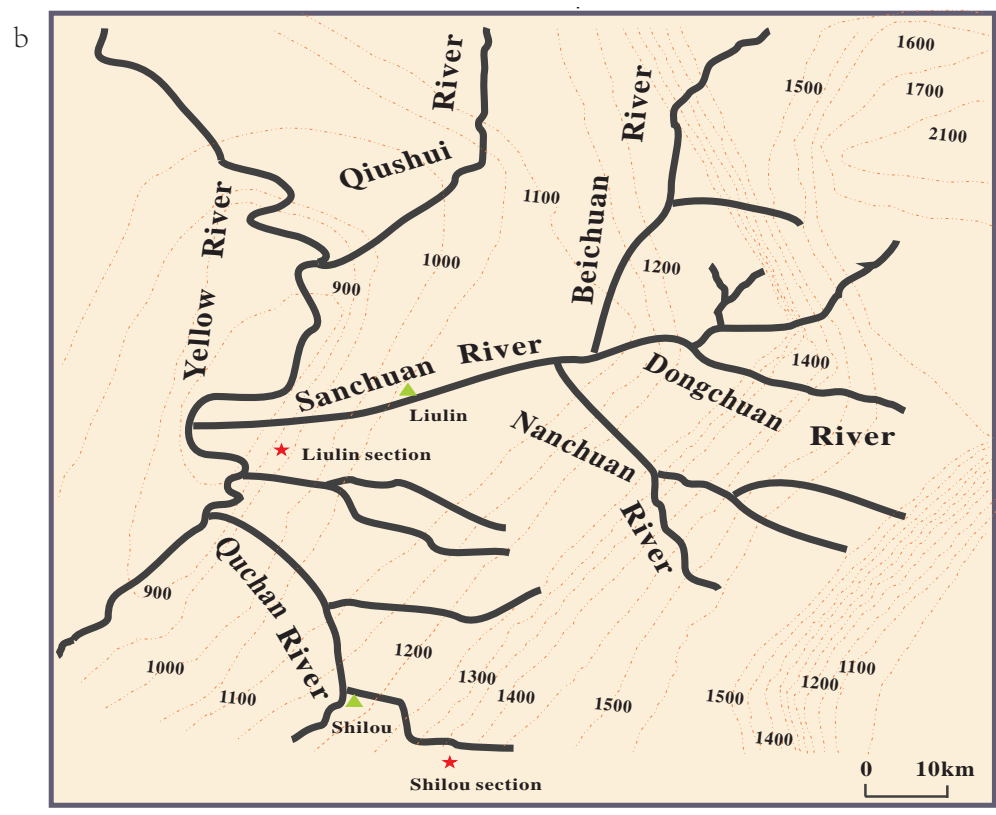
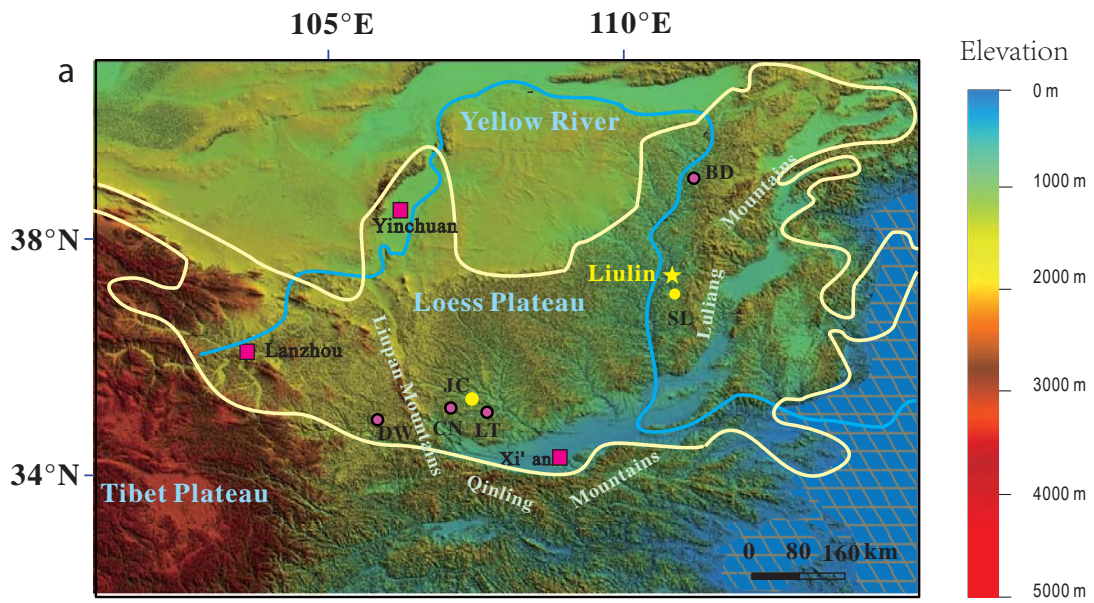


Figure 2.

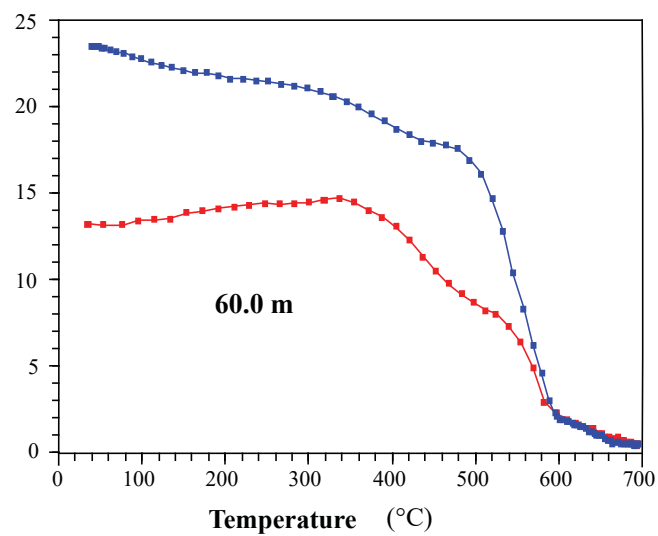
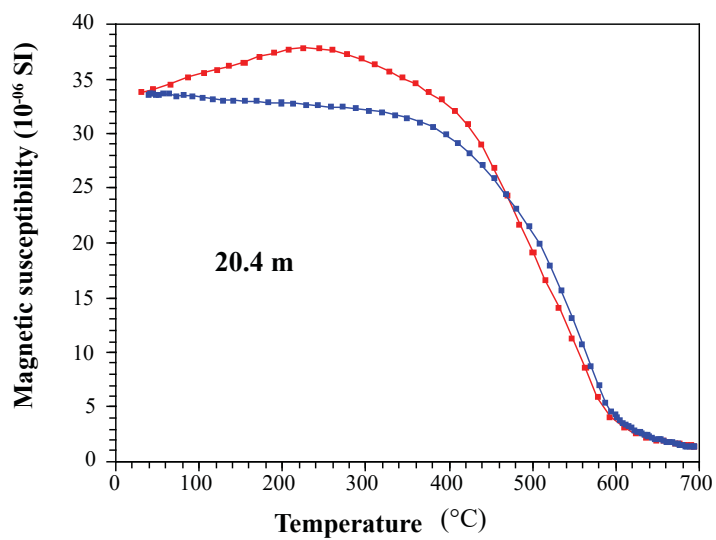
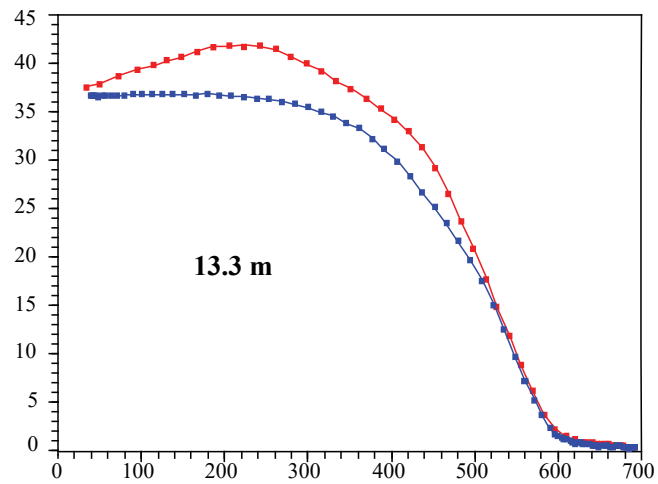
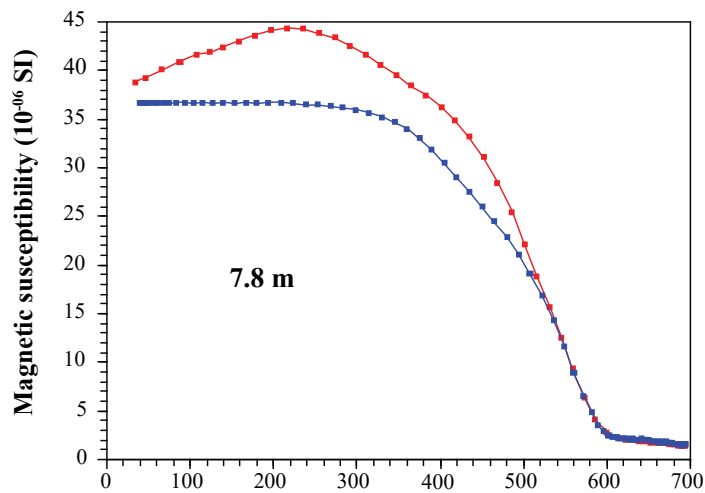


Figure 3.

● horizontal component
○ vertical component

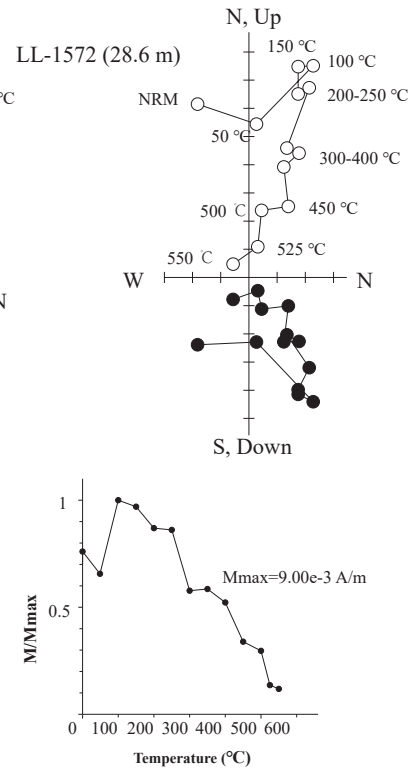
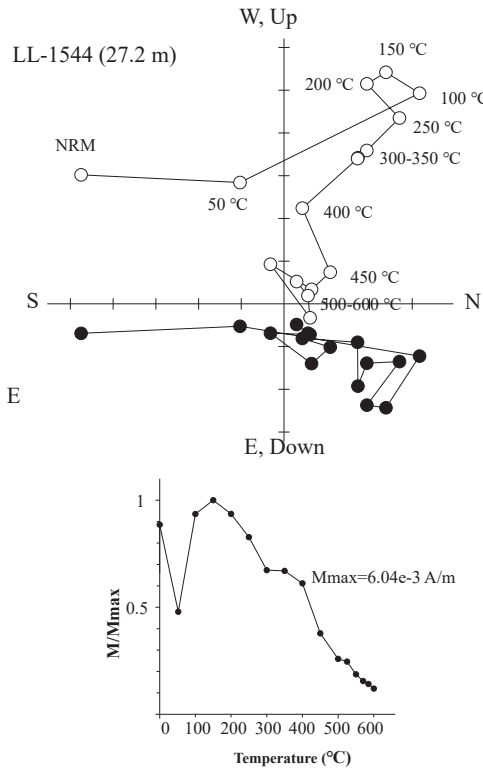
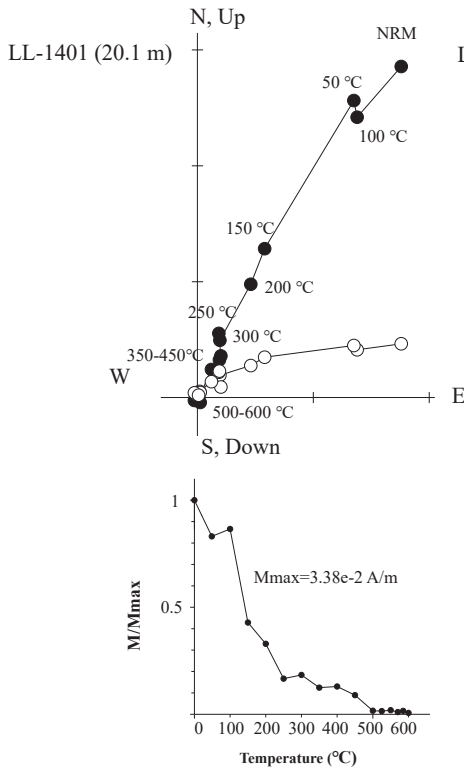
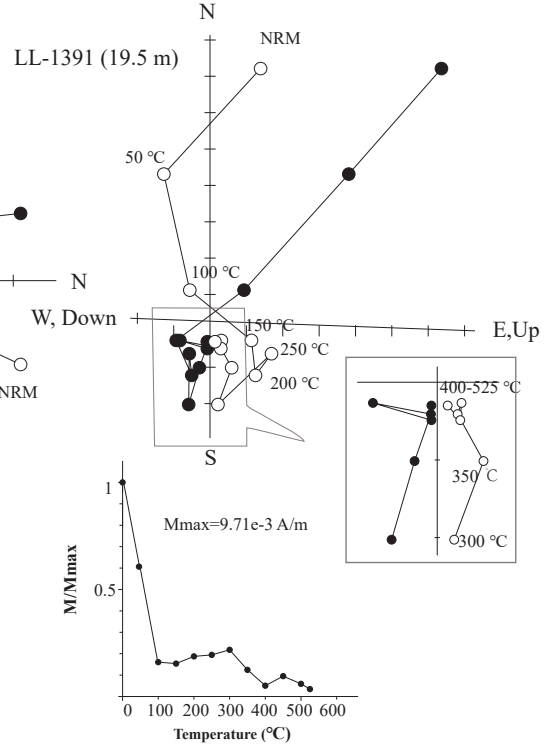
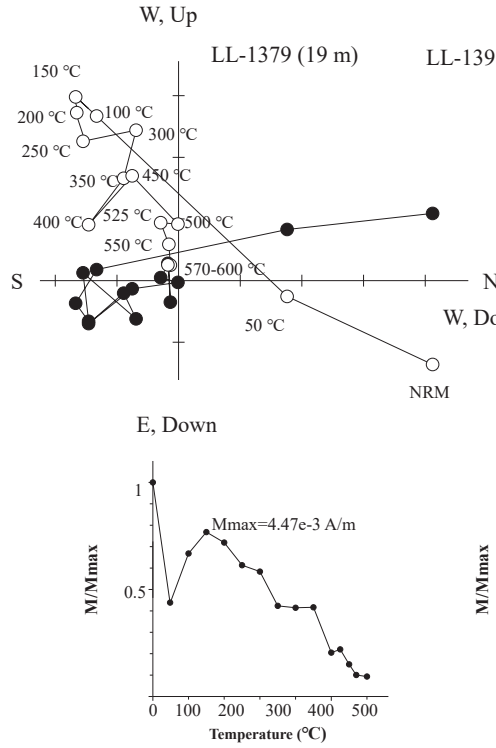
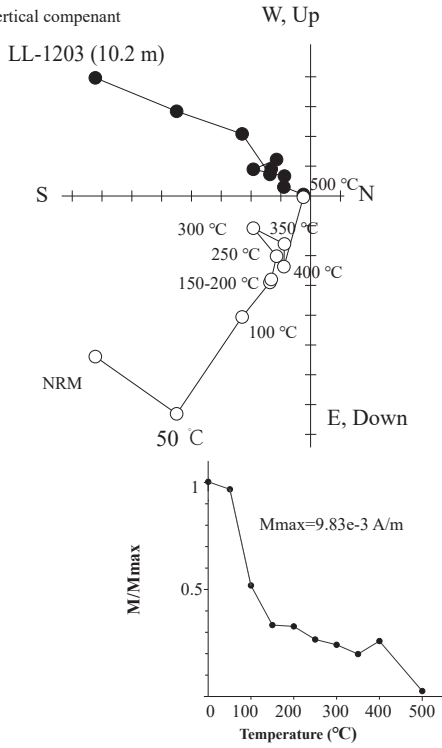


Figure 4.

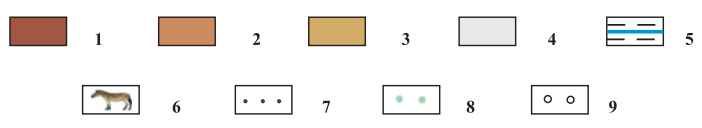
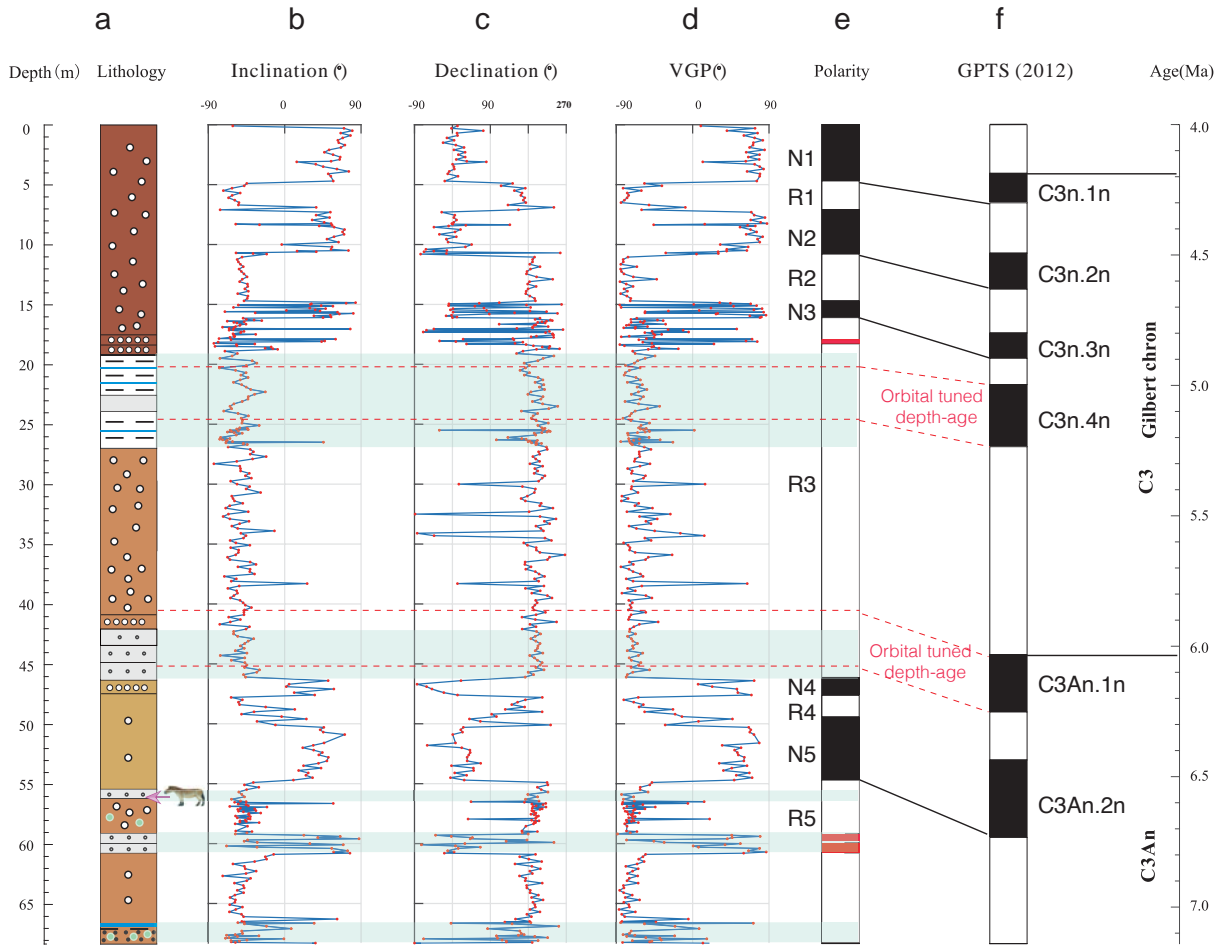


Figure 5.

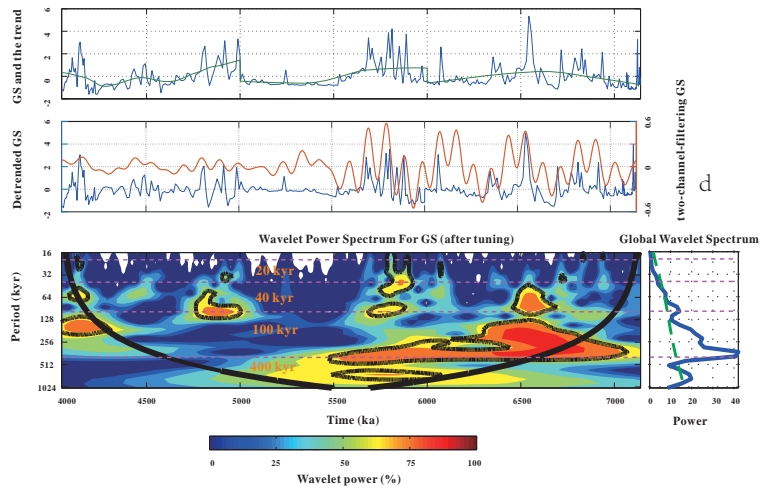
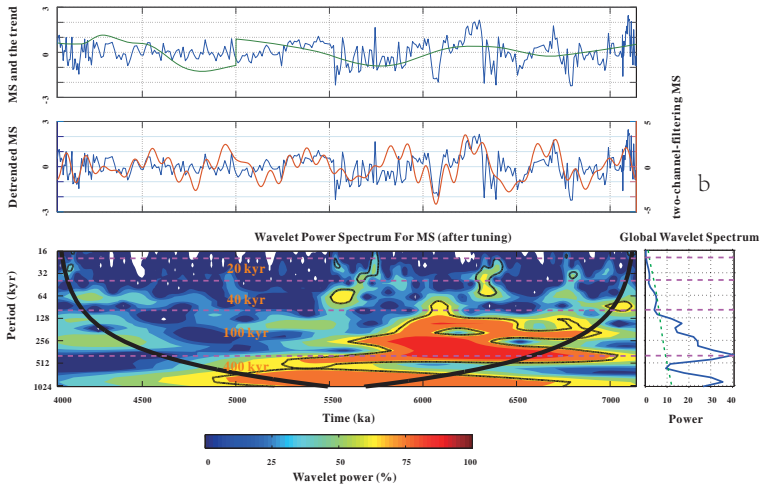
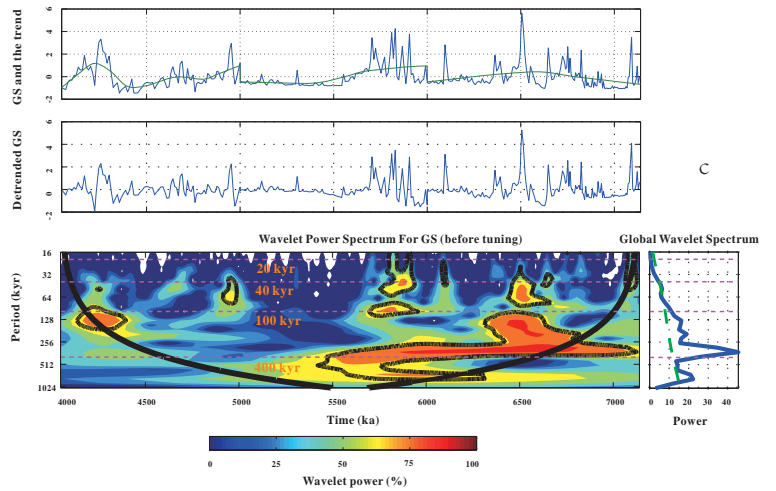
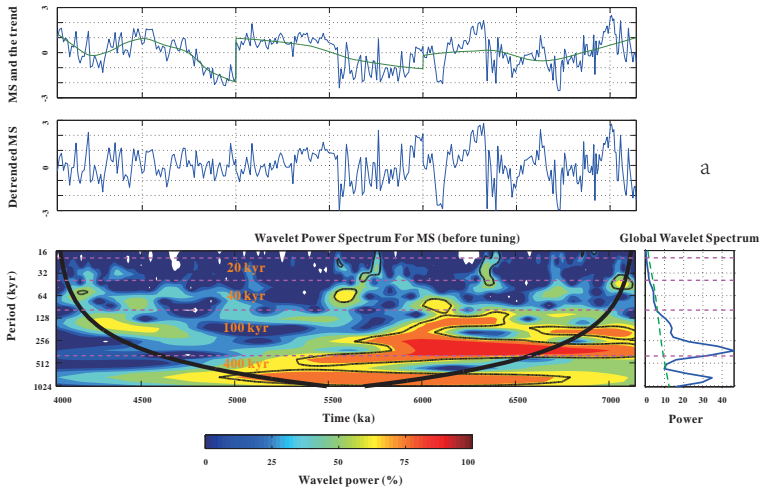
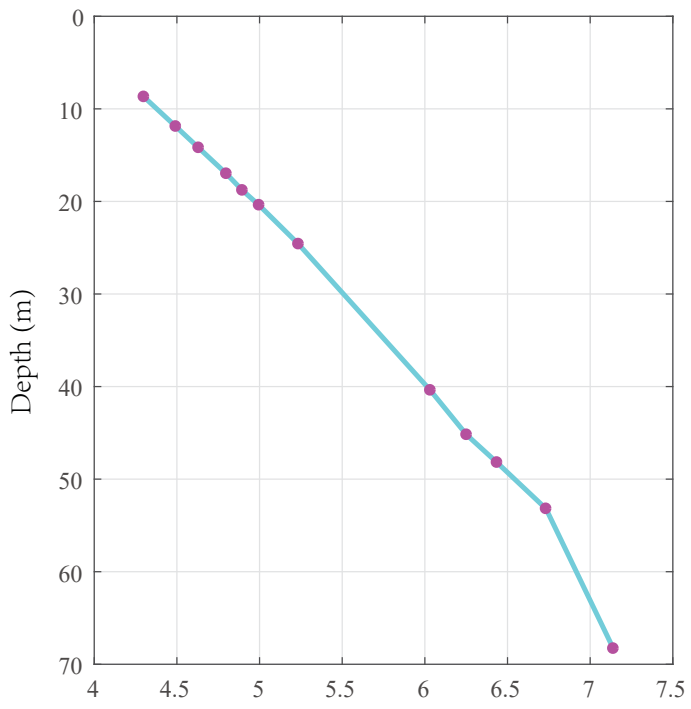


Figure 6.

Age (Ma)



Age (Ma)

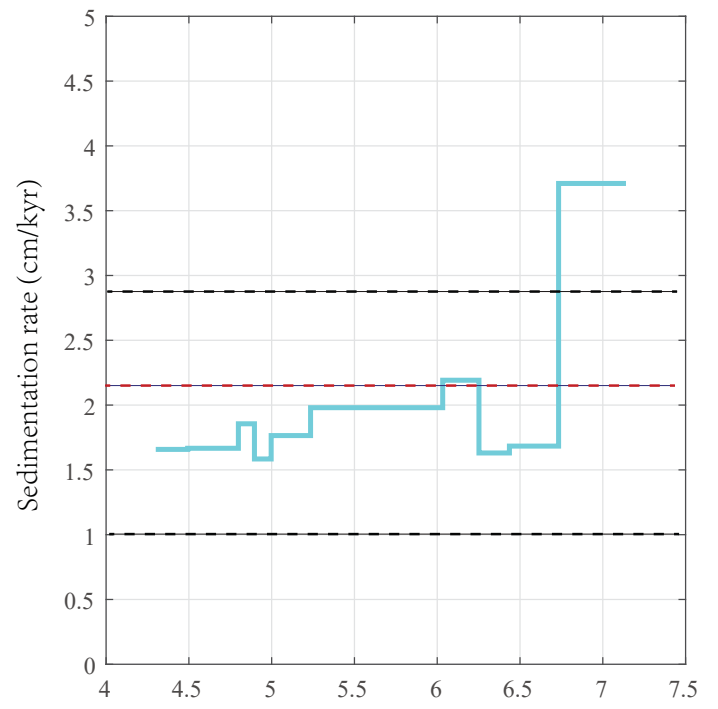


Figure 7.

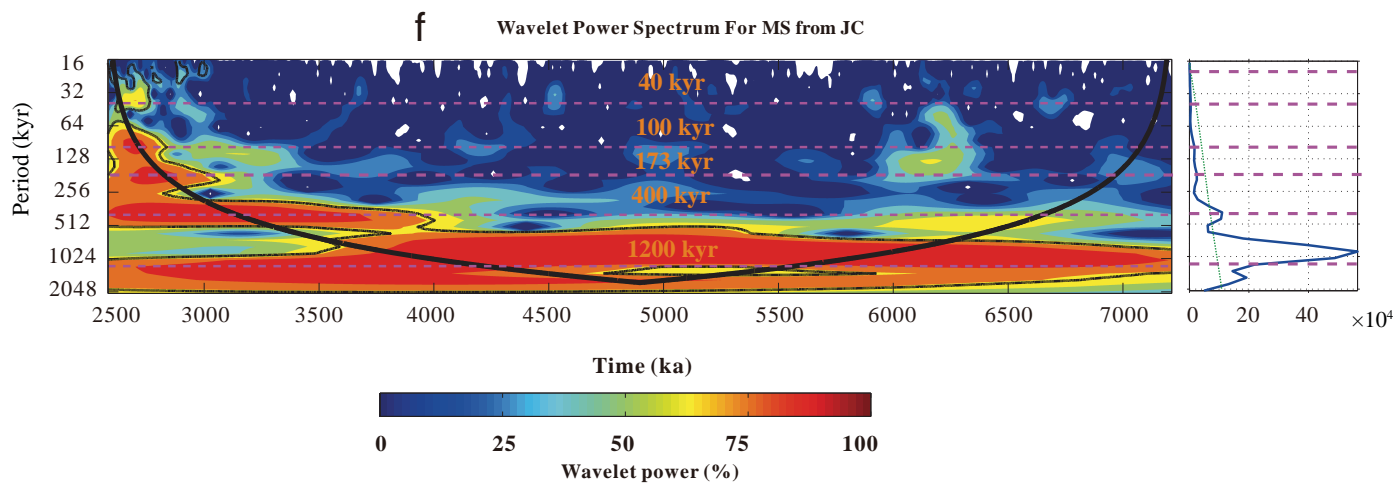
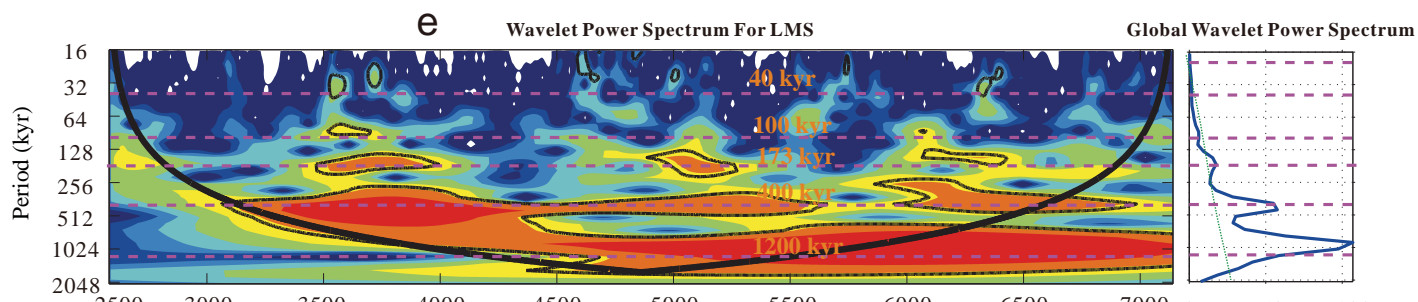
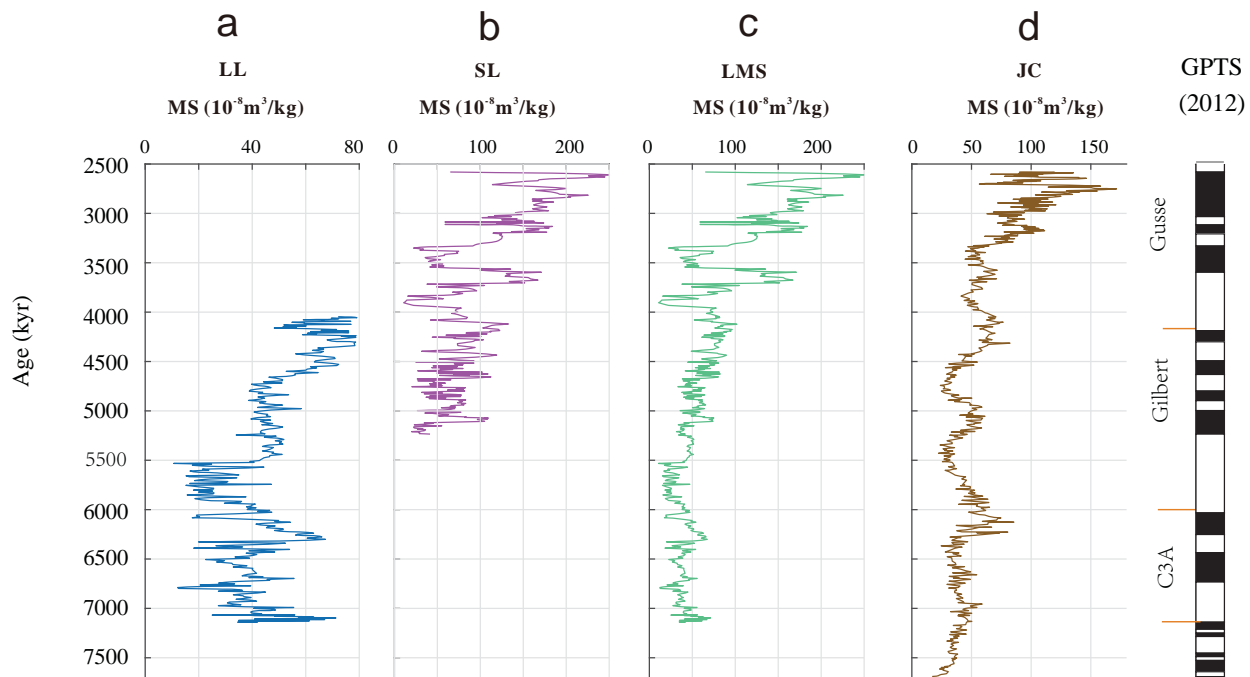


Figure 8.

3000 3500 4000 4500 5000 5500 6000 6500 7000 7500

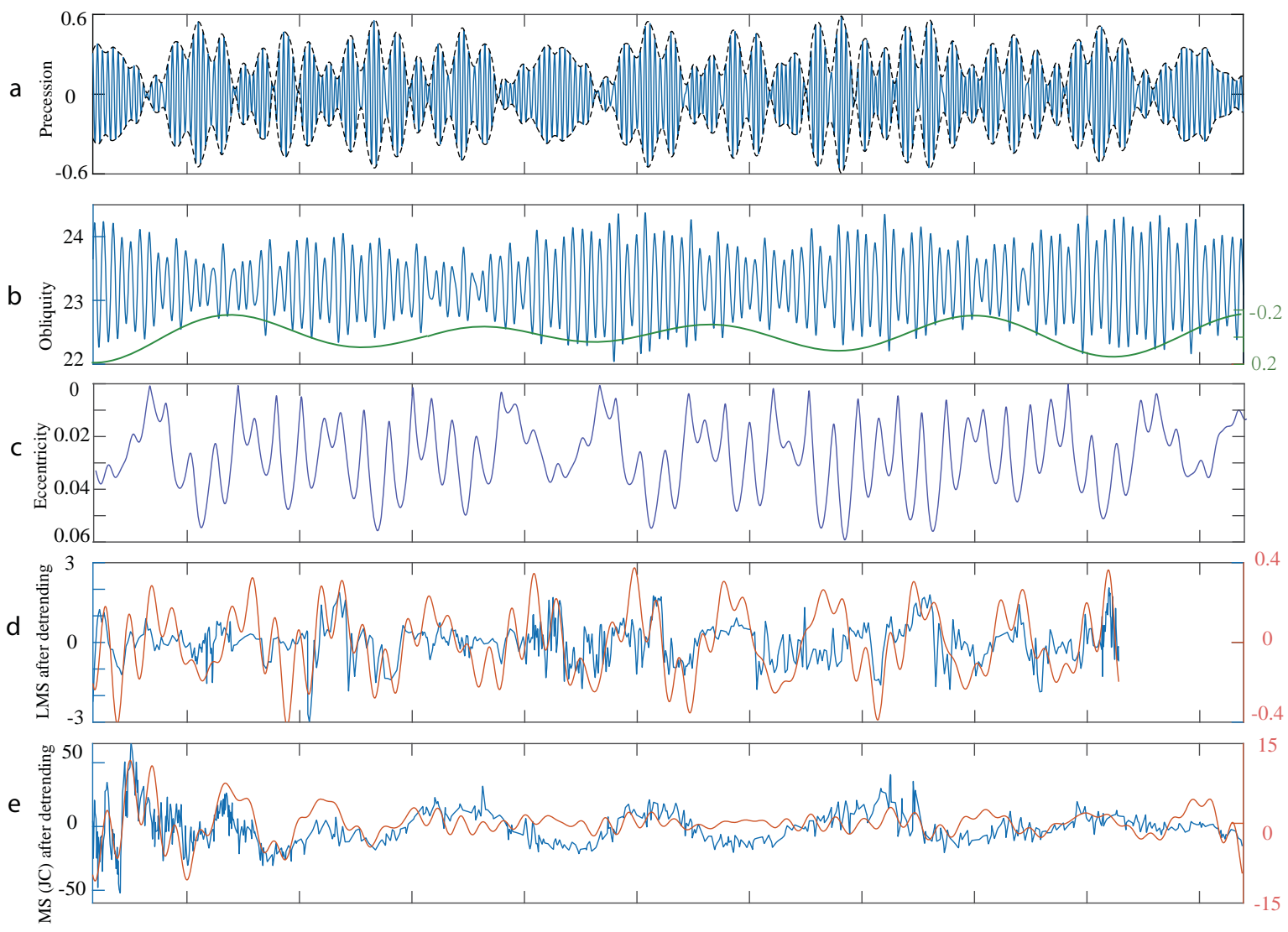


Figure 9.

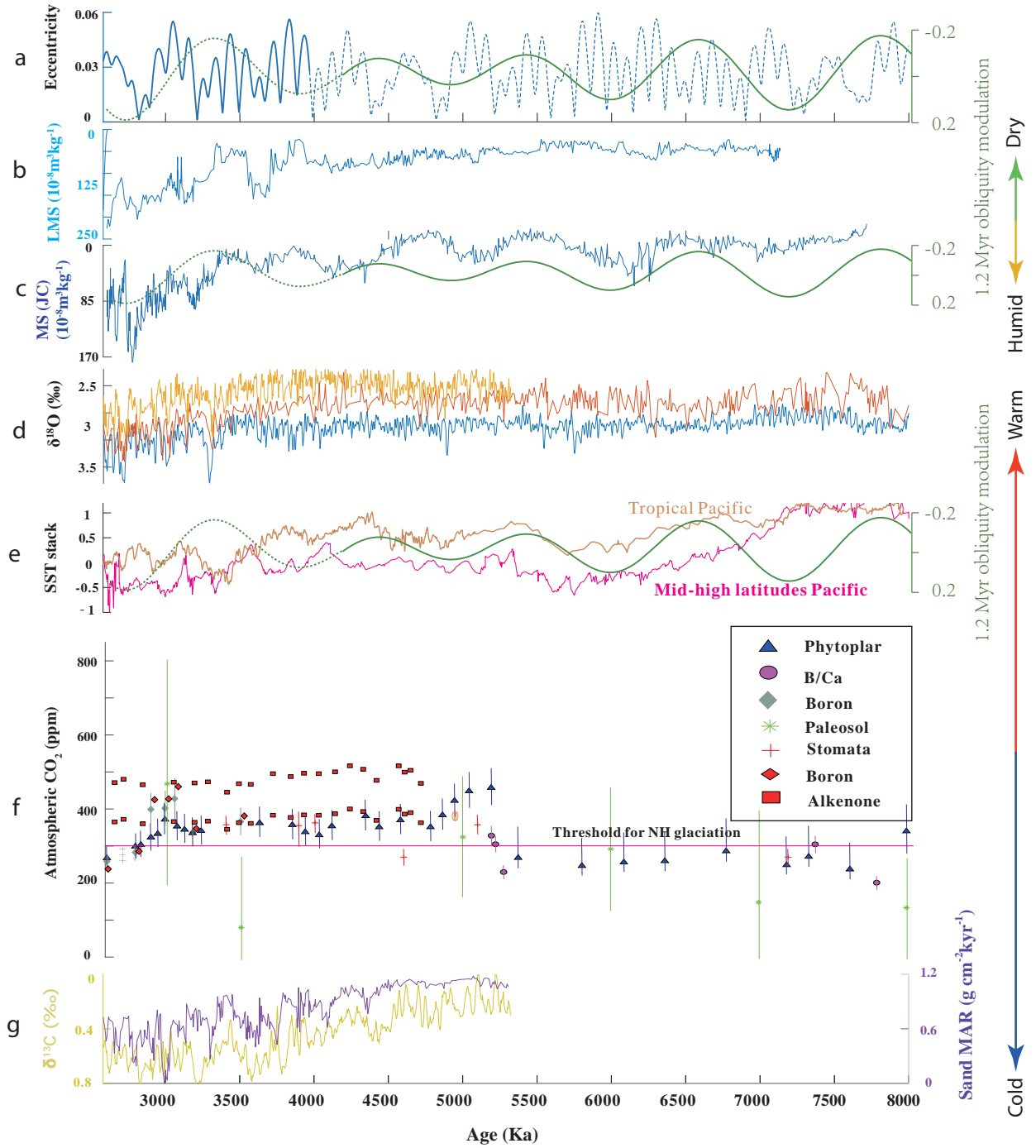


Figure 10.

